

# UC Santa Cruz

## UC Santa Cruz Previously Published Works

### Title

Equation of state and spin crossover of (Mg,Fe)O at high pressure, with implications for explaining topographic relief at the core-mantle boundary

### Permalink

<https://escholarship.org/uc/item/9w90d7bz>

### Journal

American Mineralogist, 101(5)

### ISSN

0003-004X

### Authors

Solomatova, NV  
Jackson, JM  
Sturhahn, W  
[et al.](#)

### Publication Date

2016-05-01

### DOI

10.2138/am-2016-5510

Peer reviewed

## Equation of state and spin crossover of (Mg,Fe)O at high pressure, with implications for explaining topographic relief at the core-mantle boundary

NATALIA V. SOLOMATOVA<sup>1,\*</sup>, JENNIFER M. JACKSON<sup>1</sup>, WOLFGANG STURHAHN<sup>1</sup>, JUNE K. WICKS<sup>1,2</sup>, JIYONG ZHAO<sup>3</sup>, THOMAS S. TOELLNER<sup>3</sup>, BORA KALKAN<sup>4,†</sup>, AND WILLIAM M. STEINHARDT<sup>1,5</sup>

<sup>1</sup>Seismological Laboratory, Caltech, Pasadena, California 91125, U.S.A.

<sup>2</sup>Department of Geosciences, Guyot Hall, Princeton University, Princeton, New Jersey 08544, U.S.A.

<sup>3</sup>Advanced Photon Source, Argonne National Laboratory, Argonne, Illinois 60439, U.S.A.

<sup>4</sup>Advanced Light Source, Lawrence Berkeley National Laboratory, Berkeley 94720, California, U.S.A.

<sup>5</sup>Earth & Planetary Sciences, Harvard University, Cambridge, Massachusetts 02138, U.S.A.

### ABSTRACT

Iron-bearing periclase is thought to represent a significant fraction of Earth's lower mantle. However, the concentration of iron in (Mg,Fe)O is not well constrained at all mantle depths. Therefore, understanding the effect of iron on the density and elastic properties of this phase plays a major role in interpreting seismically observed complexity in the deep Earth. Here we examine the high-pressure behavior of polycrystalline (Mg,Fe)O containing 48 mol% FeO, loaded hydrostatically with neon as a pressure medium. Using X-ray diffraction and synchrotron Mössbauer spectroscopy, we measure the equation of state to about 83 GPa and hyperfine parameters to 107 GPa at 300 K. A gradual volume drop corresponding to a high-spin (HS) to low-spin (LS) crossover is observed between ~45 and 83 GPa with a volume drop of 1.85% at 68.8(2.7) GPa, the calculated spin transition pressure. Using a newly formulated spin crossover equation of state, the resulting zero-pressure isothermal bulk modulus  $K_{0,HS}$  for the HS state is 160(2) GPa with a  $K'_{0,HS}$  of 4.12(14) and a  $V_{0,HS}$  of 77.29(0) Å<sup>3</sup>. For the LS state, the  $K_{0,LS}$  is 173(13) GPa with a  $K'_{0,LS}$  fixed to 4 and a  $V_{0,LS}$  of 73.64(94) Å<sup>3</sup>. To confirm that the observed volume drop is due to a spin crossover, the quadrupole splitting (QS) and isomer shift (IS) are determined as a function of pressure. At low pressures, the Mössbauer spectra are well explained with two Fe<sup>2+</sup>-like sites. At pressure between 44 and 84, two additional Fe<sup>2+</sup>-like sites with a QS of 0 are required, indicative of low-spin iron. Above 84 GPa, two low-spin Fe<sup>2+</sup>-like sites with increasing weight fraction explain the data well, signifying the completion of the spin crossover. To systematically compare the effect of iron on the equation of state parameters for (Mg,Fe)O, a spin crossover equation of state was fitted to the pressure-volume data of previous measurements. Our results show that  $K_{0,HS}$  is insensitive to iron concentration between 10 to 60 mol% FeO, while the spin transition pressure and width generally increases from about 50–80 and 2–25 GPa, respectively. A key implication is that iron-rich (Mg,Fe)O at the core-mantle boundary would likely contain a significant fraction of high-spin (less dense) iron, contributing a positive buoyancy to promote observable topographic relief in tomographic images of the lowermost mantle.

**Keywords:** (Mg,Fe)O, ferropericlase, spin crossover, equation of state, X-ray diffraction, synchrotron Mössbauer spectroscopy, lower mantle, ultralow-velocity zones

### INTRODUCTION

Earth's lower mantle occupies more than half of Earth's volume and is expected to be composed primarily of bridgmanite, calcium silicate perovskite, and iron-bearing periclase. Although it is suggested that (Mg,Fe)O ("ferropericlase") represents a significant volume fraction of Earth's interior, the concentration of iron in (Mg,Fe)O at conditions considered to be present in the lower mantle is largely uncertain and not very well constrained by known data. Just above the core-mantle boundary, an enhanced iron content may be found due to melting events in Earth's his-

tory and/or reactions with the iron-dominated liquid outer core. In this region, seismologists have observed 5–40 km thick patches of ultralow-velocity zones (ULVZs), often located at the edges of large low shear velocity provinces (Garnero and Helmberger 1996; McNamara et al. 2010; Rost 2013). These zones are thought to be composed of an iron-bearing layer of FeO and FeSi (Manga and Jeanloz 1996), iron-rich (Mg,Fe)O (Wicks et al. 2010, 2015; Bower et al. 2011), iron-rich (Mg,Fe)SiO<sub>3</sub> post-perovskite (Mao et al. 2004), subducted banded iron formations (Dobson and Brodholt 2005), and/or partial melt (Williams and Garnero 1996; Mosenfelder et al. 2009).

Periclase and wüstite are two end-members of the MgO-FeO solid solution with magnesiowüstite describing the iron-rich compositions and ferropericlase the magnesium-rich compositions.

\* E-mail: nsolomat@caltech.edu

† Present address: Advanced Materials Research Laboratory, Department of Physics Engineering, Hacettepe University, Beytepe 06800, Ankara, Turkey.

Under lower mantle conditions, iron is expected to be preferentially incorporated into ferropericlae when in the presence of bridgmanite and magnesium silicate post-perovskite (Kobayashi et al. 2005; Auzende et al. 2008; Sinmyo et al. 2008; Sakai et al. 2009). However, there is disagreement in the experimental and computational data for the (Mg,Fe)O solid solution regarding magnetic ordering, spin crossovers, and phase transitions (Badro et al. 2003; Lin et al. 2005, 2007; Kantor et al. 2006). At ambient conditions, (Mg,Fe)O exhibits the space group  $Fm\bar{3}m$  with  $Mg^{2+}$  and high-spin  $Fe^{2+}$  atoms located in octahedral coordination environments. Periclae (MgO) remains cubic ( $B1$ ) throughout the Earth's mantle pressures and temperatures (Duffy and Ahrens 1993), while wüstite (FeO) experiences a rhombohedral distortion at upper mantle pressures and transforms to the  $B8$  structure at pressures of the lower mantle (Yagi et al. 1985; Fei and Mao 1994; Mao et al. 2002; Fischer et al. 2011). For iron-rich (Mg,Fe)O, the rhombohedral distortion may be coupled to a magnetic-ordering transition from a paramagnetic (disordered) to antiferromagnetic (oppositely ordered) state (Mao et al. 1996; Speziale et al. 2005; Fujii et al. 2011; Zhang et al. 2012). However, it is uncertain if (Mg,Fe)O with 48 mol% FeO experiences a rhombohedral and/or magnetic-ordering transition.

At higher pressures, it is known that iron in iron-poor (Mg,Fe)O undergoes a spin crossover, resulting in a  $\sim 10\%$  decrease in iron's ionic radius (Tsuchiya et al. 2006). A reduction in volume for iron-poor (Mg,Fe)O has been shown to affect seismically relevant properties, such as sound velocities and density (Antonangeli et al. 2011; Jackson et al. 2006; Lin et al. 2006b; Marquardt et al. 2009a, 2009b). The spin crossover pressure is a function of iron concentration in ferropericlae (Sturhahn et al. 2005; Tsuchiya et al. 2006; Persson et al. 2006; Fei et al. 2007); however, scatter in reported transition pressures is large. Additionally, there is uncertainty about the effect of temperature on the spin transition pressure and broadness of the crossover. Probing the entire solid solution of (Mg,Fe)O is essential for our understanding of the behavior of iron within the ferropericlae lattice. In this study, we use X-ray diffraction and synchrotron Mössbauer spectroscopy to determine the high-pressure equation of state and hyperfine parameters for (Mg,Fe)O containing 48 mol% FeO.

## EXPERIMENTAL METHODS

The polycrystalline (Mg,Fe)O sample was synthesized by grinding together  $^{57}Fe_2O_3$  and MgO and then firing the powder in an  $H_2/CO_2$  gas-mixing furnace for about 20 h at 1400 °C, after which it was reground and reheated for an additional 20 h at the same temperature with the same  $H_2/CO_2$ . The measured oxygen fugacity,  $\log(f_{O_2})$  was about  $-0.9$ . Electron microprobe analysis identifies the composition as  $(Mg_{0.490(3)}Fe_{0.483(2)}Ti_{0.027(5)})O$ , hereafter referred to as Fp48. Titanium originated from the  $^{57}Fe_2O_3$  starting material purchased from AMT Ventures Pte, Ltd.

### X-ray diffraction

The isothermal equation of state for Fp48 was determined using X-ray diffraction at 300 K. A symmetric diamond-anvil cell was prepared with two beveled anvils, each with 300  $\mu m$  culet diameters, mounted with epoxy on WC backing plates. A 130  $\mu m$  hole with a pre-indented thickness of 43  $\mu m$  was drilled in a rhenium gasket. Polycrystalline Fp48 was ground to a fine powder, pressed into a 10  $\mu m$  thick pellet ( $\sim 40 \times 40 \mu m^2$ ), then loaded on the diamond culet and two 11  $\mu m$  ruby spheres were loaded on the opposing diamond anvil. Neon was loaded into the sample chamber using a newly designed gas-loading system at Caltech. After the sample chamber was loaded with neon, the gasket hole diameter decreased to 90  $\mu m$ .

High-pressure X-ray diffraction experiments were conducted at Beamline 12.2.2 at the Advanced Light Source (ALS) of Lawrence Berkeley National Laboratory.

The incident energy was set to 30 keV ( $\lambda = 0.41328 \text{ \AA}$ ) with a beam full-width at half maximum of about 10 by 10  $\mu m^2$ . A high-resolution image plate (MAR345) was used to collect diffraction patterns. The calibration standard used was LaB<sub>6</sub>. A fine grid was sampled throughout the sample chamber until the optimal XRD pattern was collected. X-ray diffraction patterns were collected at 44 different pressures, in intervals of 1–2 GPa from 7.5–82.9 GPa with an average pressure drift of 0.4 GPa. Ex situ pressure determinations were collected on the two rubies before and after each set of XRD measurements, using the ruby fluorescence pressure scale reported in Jacobsen et al. (2008). XRD patterns were integrated with FIT2D (Hammersley et al. 1996) and analyzed with the curve-fitting program, Fityk (Wojdyr 2010). Pressure errors for the ALS XRD experiments were determined from the standard deviation between the four ruby measurements. The 111 reflection was not resolvable at all pressures, either due to peak overlap or oversaturation on the image plate and was thus not included in this analysis. An ambient diffraction pattern was collected at Sector 11-BM of the Advanced Photon Source at Argonne National Laboratory, using a calibrated incident energy of 27 keV (0.45900  $\text{\AA}$ ). Powdered Fp48 was loaded into a Kapton capillary tube between amorphous silica such that only the Fp48 sample was in the beam path.

### Synchrotron Mössbauer spectroscopy

The hyperfine interactions, namely the quadrupole splitting and isomer shift, of Fp48 were determined with synchrotron Mössbauer spectroscopy (SMS). The isomer shift is proportional to the  $s$ -electron density at the nucleus, and hence is indirectly influenced, via shielding effects, by the  $d$ -electron population in the valence shell. The isomer shift thus provides information that helps determine the valence (i.e., oxidation) state. A quadrupole splitting is observed when an inhomogeneous electric field at the Mössbauer nucleus is present. In general, two factors can contribute to the electric field gradient, an electron distribution in the valence shell and/or a nearby, lattice environment with non-cubic symmetry. Thus, the quadrupole splitting yields information on local structure and, complementary to the isomer shift, the oxidation state and spin state.

A diamond-anvil cell was assembled with two beveled 250  $\mu m$  diamonds on WC seats for the SMS measurements. A rhenium gasket was prepared by drilling a hole with a 50  $\mu m$  thickness and 80  $\mu m$  diameter, which was then loaded with a powdered Fp48 sample (with a 10–20  $\mu m$  grain size). A 10  $\mu m$  ruby sphere was placed on the other diamond culet as a pressure gauge. Upon gas-loading the sample chamber with neon at Caltech, the gasket hole diameter decreased to  $\sim 65 \mu m$ .

The SMS measurements were conducted at Sector 3-ID-B of the Advanced Photon Source (APS). The storage ring was operated in top-up mode with 24 bunches separated by 153 ns. A high-resolution monochromator was tuned around the nuclear resonance energy of  $^{57}Fe$  with a FWHM of 1 meV (Toellner 2000). An APD detector was positioned downstream in the forward direction to measure the time spectra. X-ray energy was tuned to 14.4125 keV (the  $^{57}Fe$  nuclear transition energy). The beam was focused to an area of 10 by 11  $\mu m^2$  using a Kirkpatrick-Baez mirror system (Zhang et al. 2015). A time window of 20 to  $\sim 130$  ns after excitation was used to observe nuclear resonant scattering and fit the data. At each compression point, an SMS spectrum was collected for the sample with and without  $^{57}Fe$ -enriched stainless steel (SS) foil with a physical thickness of 2  $\mu m$ . The stainless steel foil is placed in the downstream direction as a reference absorber for isomer shift measurements. The isomer shift between the SS foil and  $\alpha$ -iron metal was measured to be  $-0.1225(9)$  mm/s. To achieve high-statistical quality spectra, collection time ranged from about 30 min with the SS foil to 45 min without the SS foil. Pressure was measured before and after the SMS data collection with ruby fluorescence at GSE-CARS of the APS. The average pressure drift was 0.5 GPa. Decompression SMS data were collected for the DAC from our ALS XRD experiments. The sample was decompressed from  $\sim 84$  to 61 GPa with an average pressure interval of 5.8 GPa.

## RESULTS

### X-ray diffraction

Representative integrated XRD patterns for Fp48 are shown in Figure 1, and calculated volumes and densities are reported in Table 1. Although the FWHM values are scattered at low pressures and display a shallow slope at high pressure (Fig. 2), we did not observe the splitting of any ferropericlae reflection peaks, suggesting that there was no structural transition. In the studied pressure range, the XRD patterns included a couple of saturated reflections, which we unsuccessfully attempted to analyze as peak broadening

due to a rhombohedral distortion. Thus, Fp48 likely remains in the B1 structure up to at least 83 GPa. Above about 45 GPa, a gradual change in the trend of volume compression is observed, suggesting the onset of an electronic spin crossover from high-spin (HS) to low-spin (LS) octahedrally coordinated  $\text{Fe}^{2+}$  (Fig. 3).

A Birch-Murnaghan spin crossover equation of state (EOS) was fitted to our data with MINUTI 1.1.2 (Chen et al. 2012; Sturhahn 2015). We fitted the HS zero-pressure volume ( $V_{0,\text{HS}}$ ), HS zero-pressure isothermal bulk modulus ( $K_{0,\text{HS}}$ ), HS zero-pressure bulk modulus derivative ( $K'_{0,\text{HS}}$ ), LS zero-pressure volume ( $V_{0,\text{LS}}$ ), LS zero-pressure isothermal bulk modulus ( $K_{0,\text{LS}}$ ) and the transition

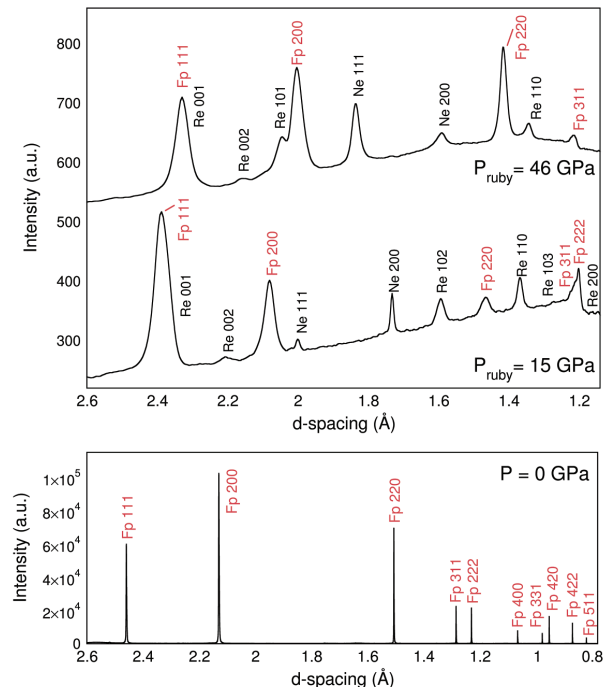


**FIGURE 1.** Integrated X-ray diffraction patterns for Fp48 at 0, 15, and 46 GPa at room temperature before background subtraction, where patterns are shifted vertically for clarity. Fp48, neon, and rhenium peaks are labeled. The ambient pattern was collected at sector 11-BM at the APS ( $\lambda = 0.45900 \text{ \AA}$ ) while patterns at pressure were collected at sector 12.2.2 at the ALS ( $\lambda = 0.41328 \text{ \AA}$ ).

pressure ( $P_T$ ). A 1.85% volume drop is calculated at 68.8(2.7) GPa, the spin transition pressure where the volume change due to the HS to LS transition is 50% complete. The zero-pressure bulk modulus  $K_{0,\text{HS}}$  for the HS state is 160(2) GPa with a  $K'_{0,\text{HS}}$  of 4.12(14) and a unit-cell  $V_{0,\text{HS}}$  of 77.29(0)  $\text{\AA}^3$ . For the LS state, the fit parameters,  $K_{0,\text{LS}}$  and  $V_{0,\text{LS}}$  are 173(13) GPa and 73.64(94)  $\text{\AA}^3$ , respectively. Fit parameter  $K'_{0,\text{LS}}$  was fixed at 4, as it was not constrained by the data. Parameter correlations and fit procedure are described in Table 2. The volume, isothermal bulk modulus, bulk sound velocity, and density are reported as a function of pressure up to 140 GPa in Table 3 with associated errors that consider parameter correlations. A plot of normalized pressure ( $F$ ) vs. Eulerian strain ( $f$ ) illustrates the change in compression behavior that occurs through the spin crossover (Fig. 3 inset). The normalized pressure decreases with increasing Eulerian strain in the spin crossover region. The onset of the spin crossover of Fp48 in this study is similar to the crossover pressures of previous studies of ferroperricite with iron concentrations of 35–50 mol% (Speziale et

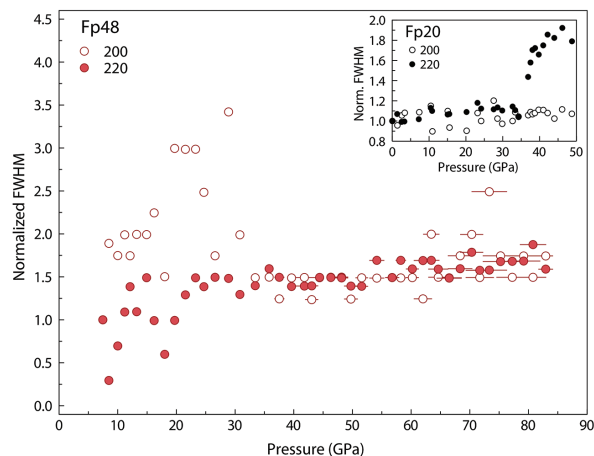


**FIGURE 2.** The full-width at half maximum (FWHM) of the 200 and 220 reflections for Fp48 from ALS XRD experiments, normalized to the lowest pressure value collected at ALS (7.46 GPa). Although the FWHM values are scattered at low pressures, no steep broadening that would be associated with a rhombohedral distortion is observed for the 220 reflection. Inset shows 220 peak broadening for Fp20 compressed without a pressure medium (Kantor et al. 2006).

**TABLE 1.** Compression data from XRD measurements of Fp48 at 300 K

$P$ (GPa)	$V$ ( $\text{\AA}^3$ )	$\rho$ ( $\text{g/cm}^3$ )	$P$ (GPa)	$V$ ( $\text{\AA}^3$ )	$\rho$ ( $\text{g/cm}^3$ )	$P$ (GPa)	$V$ ( $\text{\AA}^3$ )	$\rho$ ( $\text{g/cm}^3$ )
0.0(0)	77.29(1)	4.862(10)	28.9(5)	67.40(12)	5.575(15)	58.2(0.7)	61.24(37)	6.136(39)
7.5(2)	73.89(45)	5.085(33)	30.8(3)	67.08(22)	5.601(22)	60.2(1.0)	60.97(63)	6.163(65)
8.5(1)	73.55(2)	5.109(10)	33.4(5)	66.19(6)	5.677(13)	62.0(1.4)	60.32(12)	6.230(17)
10.0(2)	72.92(23)	5.153(19)	35.8(6)	65.70(17)	5.720(19)	63.4(1.2)	60.09(44)	6.253(48)
11.2(6)	72.54(11)	5.180(13)	37.5(8)	65.23(18)	5.761(19)	64.6(1.6)	59.80(22)	6.284(26)
12.1(2)	72.51(2)	5.182(10)	39.6(5)	64.93(6)	5.787(13)	66.5(2.0)	59.28(51)	6.339(56)
13.2(4)	72.11(36)	5.211(28)	41.8(1.9)	64.58(9)	5.819(14)	68.3(1.9)	58.90(31)	6.380(36)
14.9(5)	71.66(44)	5.244(34)	43.1(1.0)	64.18(27)	5.855(27)	70.3(1.8)	58.49(39)	6.424(45)
16.2(3)	70.95(56)	5.296(43)	44.4(6)	64.11(22)	5.861(23)	71.7(2.2)	58.11(42)	6.467(49)
18.0(2)	70.56(35)	5.325(28)	46.3(6)	63.68(63)	5.900(59)	73.3(2.8)	57.66(37)	6.516(44)
19.7(1)	69.88(58)	5.377(46)	48.2(1.0)	63.20(25)	5.945(26)	75.2(2.8)	57.40(27)	6.546(34)
21.5(3)	69.59(65)	5.399(52)	49.8(1.0)	63.01(21)	5.963(23)	77.2(2.5)	57.05(51)	6.587(60)
23.3(5)	69.05(37)	5.442(31)	51.6(9)	62.78(49)	5.985(48)	79.2(2.6)	56.57(29)	6.642(36)
24.7(3)	68.63(12)	5.475(14)	54.2(1.1)	62.09(37)	6.051(38)	80.8(2.0)	56.43(50)	6.659(60)
26.6(4)	68.26(7)	5.505(12)	56.8(1.0)	61.63(27)	6.097(29)	82.9(1.0)	56.20(15)	6.686(22)

Notes: Ambient measurement was collected at Sector 11-BM of the Advanced Photon Source while measurements at pressure were collected at Beamline 12.2.2 at the Advanced Light Source. Note that density is calculated for a 95%  $^{57}\text{Fe}$ -enriched Fp48.

al. 2005; Fei et al. 2007; Zhuravlev et al. 2010; Chen et al. 2012), but higher than that of (Mg,Fe)O containing less iron (Marquardt et al. 2009b; Lin et al. 2005; Fei et al. 2007; Mao et al. 2011). The crossover pressure is sensitive to hydrostatic conditions and is very likely a function of iron concentration, revealed by comparison to pressure-volume data for (Mg,Fe)O with 17 and 60 mol%, as discussed below (Fig. 3).

### Synchrotron Mössbauer spectroscopy

Synchrotron Mössbauer spectroscopy (SMS) spectra were fitted with version 2.1 of the CONUSS software (Sturhahn 2000), which uses a least-square algorithm to fit iron's hyperfine parameters (e.g., isomer shift, quadrupole splitting, and distribution of the quadrupole splitting expressed as the full-width at half maximum) and material properties (e.g., effective thickness, thickness distribution, and relative weights of the sites). Typical spectra with their best-fit models are shown in Figure 4. Analysis of the SMS spectra suggests the existence of two Fe<sup>2+</sup> environments with distinguishable quadrupole splittings (QS) and similar isomer shifts (IS). One Fe<sup>2+</sup>-like site was not sufficient in describing the spectra. Attempts were made to introduce a Fe<sup>3+</sup>-like site with starting values of the QS ranging from 0 to 0.8 mm/s and IS values with respect to Fe<sup>2+</sup> of 0.4 to 0.8 mm/s. However, its weight converged to 0, suggesting the near absence of Fe<sup>3+</sup> or a quantity below the detection limit.

**TABLE 2.** Error correlation matrix for the EOS parameters fitted with MINUTI for Fp48

	$V_{0,HS}$	$K_{OT,HS}$	$K'_{OT,HS}$	$V_{0,LS}$	$K_{OT,LS}$	$P_{tr}$
$V_{0,HS}$	1.000	-0.091	0.038	0.008	-0.007	-0.010
$K_{OT,HS}$	-0.091	1.000	-0.903	-0.143	0.064	0.414
$K'_{OT,HS}$	0.038	-0.903	1.000	0.264	-0.151	-0.627
$V_{0,LS}$	0.008	-0.143	0.264	1.000	-0.984	-0.514
$K_{OT,LS}$	-0.007	0.064	-0.151	-0.984	1.000	0.376
$P_{tr}$	-0.010	0.414	-0.627	-0.514	0.376	1.000

Notes: Perfect correlation corresponds to  $\pm 1$  and a lack of correlation corresponds to 0. A prior (and prior window) of  $160 (\pm 5)$  GPa,  $170 (\pm 20)$  GPa, and  $4 (\pm 0.5)$  were used for  $K_{OT,HS}$ ,  $K_{OT,LS}$ , and  $K'_{OT,HS}$ , respectively. No priors were used for  $V_{0,LS}$  and  $P_{tr}$  and  $K_{OT,LS}$  was fixed to 4. The calculated spin transition pressure, where the volume change due to the HS to LS transition is 50% complete, is  $68.8(2.7)$  GPa. The best fit zero-pressure bulk modulus  $K_{OT,HS}$  for the HS state is  $160(2)$  GPa with a  $K'_{OT,HS}$  of  $4.12(14)$  and a unit-cell  $V_{0,HS}$  of  $77.29(0) \text{ \AA}^3$ . For the LS state,  $K_{OT,LS}$  and  $V_{0,LS}$  are  $173(13)$  GPa and  $73.64(94) \text{ \AA}^3$ , respectively.

**TABLE 3.** Volume ( $V$ ), isothermal bulk modulus ( $K_T$ ), bulk sound velocity ( $v_b$ ), and density ( $\rho$ ) as a function of pressure, obtained from fitting a spin crossover EOS to the compression data for Fp48

$P$ (GPa)	$V$ ( $\text{\AA}^3$ )	$K_T$ (GPa)	$v_b$ (km/s)	$\rho$ (g/cm <sup>3</sup> )	$P$ (GPa)	$V$ ( $\text{\AA}^3$ )	$K_T$ (GPa)	$v_b$ (km/s)	$\rho$ (g/cm <sup>3</sup> )
0	77.29(0)	160.3(1.5)	5.885(27)	4.829(9)	72	58.18(10)	273.8(13.9)	6.969(180)	6.416(17)
4	75.47(1)	176.6(1.0)	6.100(18)	4.945(10)	76	57.34(12)	283.4(16.7)	7.231(213)	6.509(18)
8	73.86(2)	192.6(0.7)	6.298(12)	5.054(10)	80	56.59(11)	327.0(25.3)	7.631(295)	6.596(18)
12	72.40(2)	208.2(0.7)	6.482(11)	5.155(10)	84	55.95(11)	381.9(24.4)	7.992(257)	6.671(19)
16	71.07(2)	223.6(0.9)	6.653(14)	5.252(10)	88	55.40(12)	427.8(19.5)	8.270(191)	6.737(20)
20	69.85(2)	238.8(1.3)	6.813(19)	5.344(11)	92	54.91(13)	462.6(15.6)	8.479(148)	6.798(20)
24	68.72(3)	253.7(1.7)	6.963(24)	5.431(11)	96	54.45(13)	489.2(13.8)	8.640(127)	6.855(21)
28	67.68(3)	268.1(2.0)	7.102(28)	5.515(11)	100	54.01(14)	510.6(13.2)	8.770(120)	6.910(22)
32	66.70(3)	282.1(2.3)	7.229(30)	5.596(11)	104	53.60(14)	528.6(13.2)	8.878(118)	6.964(23)
36	65.78(4)	295.0(2.5)	7.339(32)	5.674(11)	108	53.20(15)	544.6(13.5)	8.971(118)	7.016(24)
40	64.91(4)	306.3(2.9)	7.425(36)	5.750(12)	112	52.82(15)	559.4(13.8)	9.056(120)	7.067(24)
44	64.08(4)	314.7(4.0)	7.474(48)	5.824(12)	116	52.44(15)	573.4(14.1)	9.134(121)	7.117(25)
48	63.28(5)	317.9(6.5)	7.464(77)	5.898(12)	120	52.08(16)	586.9(14.3)	9.208(122)	7.166(26)
52	62.48(5)	312.8(10.4)	7.360(124)	5.973(13)	124	51.73(16)	600.1(14.4)	9.279(122)	7.214(27)
56	61.67(7)	297.0(13.6)	7.127(166)	6.052(14)	128	51.39(17)	613.1(14.6)	9.348(123)	7.262(28)
60	60.81(10)	275.3(11.3)	6.810(143)	6.137(15)	132	51.06(17)	626.0(14.6)	9.415(122)	7.309(29)
64	59.92(10)	266.1(12.3)	6.675(153)	6.229(16)	136	50.74(18)	638.8(14.7)	9.480(122)	7.356(29)
68	59.03(9)	272.6(12.0)	6.813(150)	6.323(16)	140	50.43(18)	651.6(15.1)	9.544(124)	7.401(30)

Notes: Cited uncertainties include parameter correlations given in Table 2. The bulk sound velocity and density were corrected for natural <sup>57</sup>Fe abundance.

At pressures below 44 GPa, our spectra were fitted with two high-spin Fe<sup>2+</sup>-like sites, distinguishable by their hyperfine fields (hereafter referred to as Fe<sub>A</sub><sup>2+</sup> and Fe<sub>B</sub><sup>2+</sup>) with a relative weight of 40 and 60%, respectively (Fig. 5; Table 4). At pressures between 44 and 84 GPa, we introduce an additional Fe<sup>2+</sup>-like site with a QS of 0 mm/s, indicative of low-spin iron. The weight of LS Fe<sup>2+</sup> increases with increasing pressure while the weight ratio of the two HS sites is preserved. This model was successfully applied

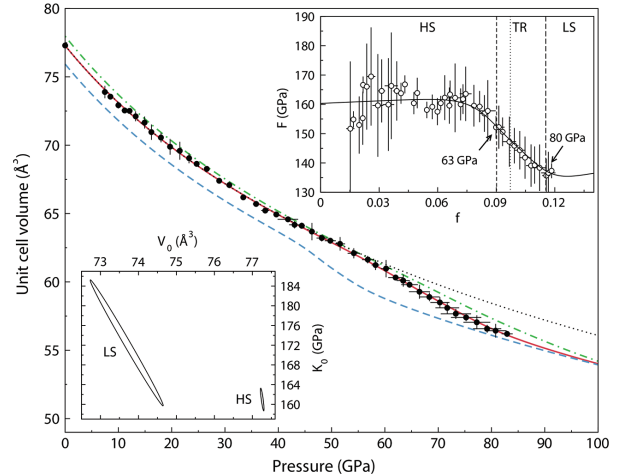


**FIGURE 3.** Pressure-volume relationship of Fp48 at 300 K, determined from the 200 and 220 reflections. The pressure standard is ruby (Jacobsen et al. 2008). The solid red and dotted black curves are the fitted spin crossover and high-spin equations of states for Fp48, respectively. The dashed blue curve and dashed dotted green curve are the spin crossover EOSs fitted with MINUTI to (Mg,Fe)O data with 17 and 60 mol% FeO (Lin et al. 2005), respectively. The upper right inset is the normalized pressure ( $F$ ) vs. Eulerian strain ( $f$ ) for Fp48. The resulting spin crossover region (TR) from the SMS fitting procedure is indicated by the vertical dashed lines, corresponding to the point at which 35% (63 GPa) and 65% (80 GPa) of the Fe<sup>2+</sup> atoms are in the LS state, respectively. The black dotted line corresponds to the spin transition pressure of 68.8 GPa, determined from the spin crossover EOS (Sturhahn 2015). The bottom left inset shows the covariance ellipses (68% confidence regions) for the HS and LS states for the parameters,  $K_{OT}$  and  $V_0$ , where  $K'_{OT,LS}$  was fixed to 4.

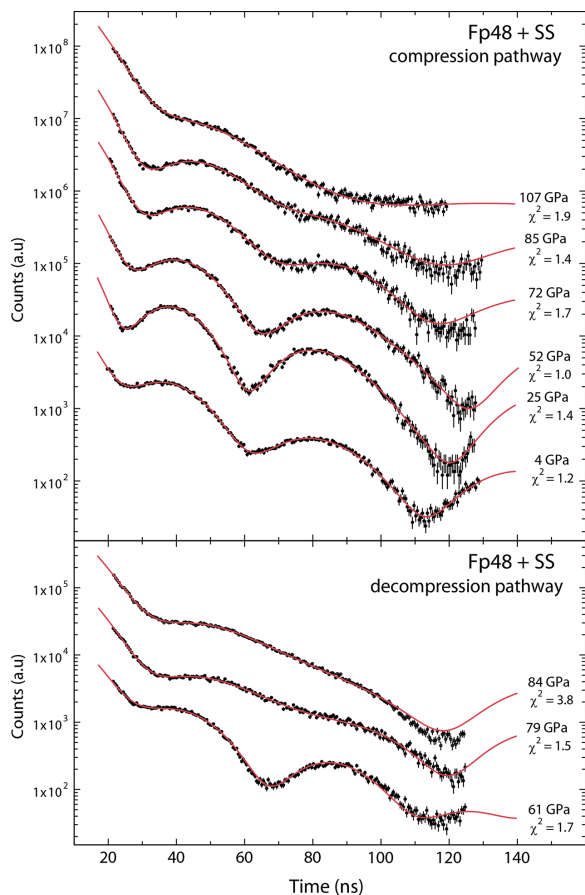


**FIGURE 4.** Representative SMS spectra and their best-fit models using CONUSS, collected at 3-ID-B of the APS (compression pathway on top; decompression pathway on bottom). The influence of pressure on the spectral features is evident through the decrease of the quantum beat amplitudes with increasing pressure. The corresponding pressure and reduced  $\chi^2$  of each fit is noted to the right of each spectrum. Note that these data sets are from two different DAC preparations, each with powdered Fp48 in a Ne pressure medium (see Experimental methods).

to decompression measurements, which span the spin crossover pressure range (Table 5). Above 84 GPa, the spectra are best fit with two low-spin  $\text{Fe}^{2+}$ -like sites (with a relative weight of 40% and 60%) with identical IS values, but different IS distributions. For example, at 98 GPa, the two low-spin  $\text{Fe}^{2+}$ -like sites have an IS of 0.434(8) mm/s and a full-width at half maximum (FWHM) of 1.13 and 0.40 mm/s. The negative slope of the IS with pressure for the  $\text{Fe}^{2+}$  sites is consistent with previous studies on (Mg,Fe)O approaching a spin crossover (Kantor et al. 2006; Lin et al. 2006a) and is a result of an increase in electron density at the nucleus with increasing pressure. The CONUSS fits reveal that 50% of the  $\text{Fe}^{2+}$  atoms are in the LS state at 72 and 69 GPa in the compression and decompression pathways, respectively. These results compare well with the transition pressure of 68.8(2.7) GPa obtained from the spin crossover EOS fit with MINUTI to the pressure-volume data set of Fp48.

The SMS spectra display quantum beats originating from the QS of HS  $\text{Fe}^{2+}$  and dynamic beats due to sample thickness. Flatten-

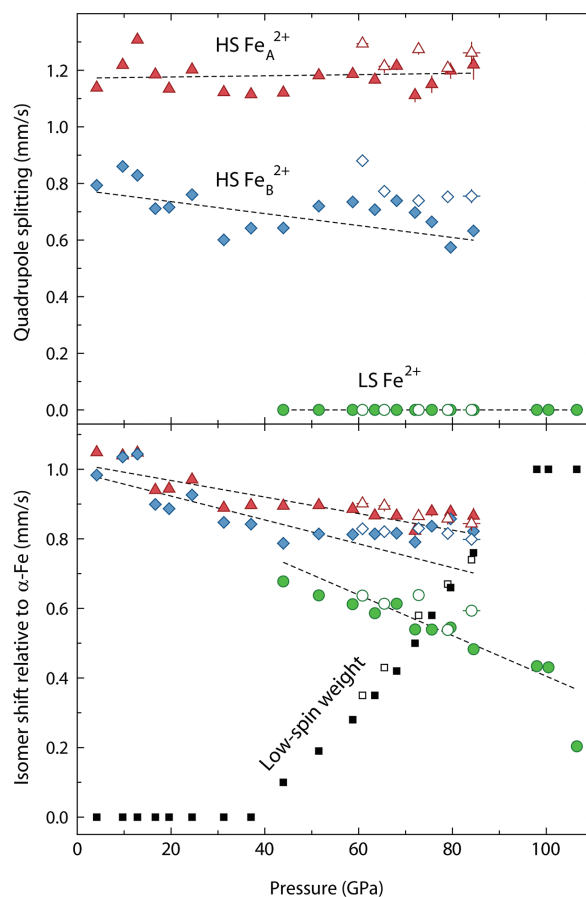


**FIGURE 5.** Quadrupole splitting and isomer shift (relative to  $\alpha$ -Fe) of Fp48. Red triangles correspond to the HS  $\text{Fe}_A^{2+}$  site, blue diamonds are the HS  $\text{Fe}_B^{2+}$  site and green circles are the LS  $\text{Fe}^{2+}$  site. Filled symbols denote hyperfine parameters acquired during compression, and open symbols denote hyperfine parameters acquired during decompression. The weight of the LS  $\text{Fe}^{2+}$  site is denoted by filled squares for the compression pathway and open squares for the decompression pathway. Dashed lines are guides for the eyes.

ing of the SMS spectra is a result of the gradual disappearance of the HS  $\text{Fe}^{2+}$  sites (QS =  $\sim 1.2$  and  $\sim 1.7$  mm/s) and the appearance of LS  $\text{Fe}^{2+}$  (QS = 0 mm/s). The quadrupole splitting is related to the amount of distortion of the coordination polyhedron. Defects within a crystal lattice can result in variations of octahedral  $\text{Fe}^{2+}$  environments (Jacobsen et al. 2002). It is possible that the presence of Ti, high Fe concentration, and/or clustering yields two dominant and unique hyperfine fields for  $\text{Fe}^{2+}$  rather than one  $\text{Fe}^{2+}$  site; however, further studies would be required to confirm this explanation. The measured values of QS and IS are consistent with high-spin  $\text{Fe}^{2+}$  in octahedral coordination environments, and we interpret the two distinct QS values to represent relatively low and high distortion, respectively, while not breaking cubic symmetry of the long-range order. No evidence of magnetic ordering was observed.

The lack of complexity in the spectra without a stainless steel reference absorber resulted in various possible solutions with nearly identical reduced  $\chi^2$ . Thus, those parameters were con-

**TABLE 4.** Best-fit hyperfine parameters for Fp48 with a stainless steel reference absorber and their corresponding reduced  $\chi^2$  for the compression pathway

P (GPa)	Fe <sub>A</sub> <sup>2+</sup> QS (mm/s)	Fe <sub>A</sub> <sup>2+</sup> FWHM (mm/s)	Fe <sub>A</sub> <sup>2+</sup> IS (mm/s)	Fe <sub>B</sub> <sup>2+</sup> QS (mm/s)	Fe <sub>B</sub> <sup>2+</sup> FWHM (mm/s)	Fe <sub>B</sub> <sup>2+</sup> IS (mm/s)	Fe <sub>LS</sub> <sup>2+</sup> weight	Fe <sub>LS</sub> <sup>2+</sup> IS (mm/s)	Fe <sub>LS</sub> <sup>2+</sup> FWHM (mm/s)	reduced $\chi^2$
4.1(1)	1.138(11)	0.58	1.049(7)	0.793(4)	0.33	0.983(3)	–	–	–	1.23
9.7(3)	1.219(11)	0.67	1.040(8)	0.859(6)	0.38	1.035(3)	–	–	–	1.67
12.8(0)	1.308(7)	0.50	1.048(5)	0.828(6)	0.38	1.044(3)	–	–	–	1.53
16.7(1)	1.185(8)	0.40	0.940(6)	0.709(5)	0.30	0.899(3)	–	–	–	1.17
19.6(7)	1.134(6)	0.45	0.944(4)	0.714(3)	0.30	0.887(2)	–	–	–	1.65
24.5(0)	1.202(8)	0.40	0.970(9)	0.758(7)	0.35	0.926(4)	–	–	–	1.36
31.2(9)	1.122(7)	0.30	0.889(5)	0.600(4)	0.20	0.847(3)	–	–	–	1.89
37.0(1)	1.115(10)	0.30	0.897(8)	0.640(6)	0.30	0.842(4)	–	–	–	1.67
43.9(3)	1.121(6)	0.40	0.895(3)	0.641(3)	0.30	0.787(1)	0.10	0.678(9)	0.60	1.62
51.5(6)	1.182(9)	0.45	0.897(5)	0.717(5)	0.32	0.814(2)	0.19	0.638(8)	0.66	0.99
58.7(6)	1.186(7)	0.38	0.886(4)	0.735(6)	0.30	0.813(2)	0.28	0.612(6)	0.86	1.34
63.4(2)	1.166(14)	0.38	0.867(9)	0.707(9)	0.35	0.814(5)	0.35	0.586(10)	0.86	1.68
68.1(1)	1.215(15)	0.30	0.867(11)	0.689(16)	0.42	0.816(11)	0.42	0.613(13)	0.86	2.08
72.0(0)	1.112(25)	0.60	0.823(15)	0.689(15)	0.43	0.791(8)	0.50	0.540(7)	0.75	1.67
75.6(2)	1.151(31)	0.65	0.879(15)	0.664(11)	0.44	0.836(7)	0.58	0.539(7)	0.91	1.50
79.6(8)	1.199(29)	0.50	0.878(13)	0.571(12)	0.35	0.857(8)	0.66	0.545(7)	0.90	1.91
84.5(6)	1.220(53)	0.50	0.866(23)	0.627(16)	0.28	0.822(8)	0.76	0.483(5)	0.80	1.43
98.0(4)	–	–	–	–	–	–	1	0.434(8)	1.13, 0.40	1.82
100.5(3)	–	–	–	–	–	–	1	0.431(11)	1.24, 0.58	1.48
106.5(7)	–	–	–	–	–	–	1	0.203(11)	1.35, 0.65	1.92

Notes: The relative weight of the Fe<sub>A</sub><sup>2+</sup> and Fe<sub>B</sub><sup>2+</sup> sites are fixed to 40 and 60%, respectively. Values in parentheses indicate the 68% uncertainty in the last digit(s). The spectra with their best-fit models at 4.1(1), 24.5(0), 51.5(6), 72.0(0), 84.5(6), and 106.5(7) GPa are shown in Figure 4. IS values are with respect to  $\alpha$ -iron metal.

**TABLE 5.** Best-fit hyperfine parameters for Fp48 with a stainless steel reference absorber and their corresponding reduced  $\chi^2$  for the decompression pathway

P (GPa)	Fe <sub>A</sub> <sup>2+</sup> QS (mm/s)	Fe <sub>A</sub> <sup>2+</sup> FWHM (mm/s)	Fe <sub>A</sub> <sup>2+</sup> IS (mm/s)	Fe <sub>B</sub> <sup>2+</sup> QS (mm/s)	Fe <sub>B</sub> <sup>2+</sup> FWHM (mm/s)	Fe <sub>B</sub> <sup>2+</sup> IS (mm/s)	Fe <sub>LS</sub> <sup>2+</sup> weight	Fe <sub>LS</sub> <sup>2+</sup> IS (mm/s)	Fe <sub>LS</sub> <sup>2+</sup> FWHM (mm/s)	Reduced $\chi^2$
84.1(1.9)	1.262(39)	0.63	0.844(21)	0.755(25)	0.18	0.798(12)	0.74	0.593(4)	0.52	3.85
79.0(3)	1.208(21)	0.73	0.858(17)	0.753(21)	0.04	0.816(11)	0.67	0.538(3)	0.50	1.48
72.8(8)	1.274(19)	0.63	0.865(12)	0.739(15)	0.18	0.830(8)	0.58	0.638(4)	0.52	2.34
65.5(1.2)	1.214(24)	0.57	0.895(16)	0.772(17)	0.10	0.821(9)	0.43	0.613(4)	0.53	1.41
60.8(1.3)	1.294(8)	0.19	0.901(7)	0.880(13)	0.28	0.829(5)	0.35	0.637(9)	0.98	1.74

Note: The spectra with their best-fit models at 60.8(1.3), 79.0(3), and 84.1(1.9) GPa are shown in Figure 4.

strained with priors derived from the fit of the sample with SS, demonstrating the necessity of performing SMS measurements with a reference absorber and the benefit of using priors. For example, during the fit of Fp48 at 12.8 GPa without SS, the priors for the Fe<sub>A</sub><sup>2+</sup> QS and Fe<sub>B</sub><sup>2+</sup> QS were set to 1.308 and 0.828 mm/s, respectively, with a window of  $\pm 0.01$  mm/s. The prior for the isomer shift between the two Fe<sup>2+</sup> sites (IS<sup>A-B</sup>) was set to 0.004 mm/s with a window of  $\pm 0.001$  mm/s. The resulting fitted values for the sample without the reference absorber were Fe<sub>A</sub><sup>2+</sup> QS = 1.301(12) mm/s, Fe<sub>B</sub><sup>2+</sup> QS = 0.8115(39) mm/s, and IS<sup>A-B</sup> = 0.0041(12) mm/s with a reduced  $\chi^2$  of 1.46. Thus, with this prior information, there was good agreement between parameters derived from fitting the sample with and without the SS reference absorber. Although individual spectra may have multiple satisfactory fits at a given pressure, the model presented here is the only self-consistent solution (i.e., a reasonable physical model that explains the data through the entire pressure range with and without a SS reference absorber). Due to the large number of parameters, the FWHM of the quadrupole splitting and the weight ratio of the Fe<sup>2+</sup>-like sites were fixed at all pressures while the effective thickness [effective thickness ( $\eta$ ) is the product of the volume density of the resonant nuclei ( $\rho$ ), nuclear resonant cross section ( $\sigma$ ), Lamb-Mössbauer factor ( $f_{LM}$ ), and the sample thickness ( $D$ )] and its distribution was fixed when three sites were used (i.e., in the spin crossover region). Fixed values were determined from Monte Carlo searches. The error correlation matrix of a typical fit within the crossover region is reported in Table 6. No strong correlations occur in this fitting procedure, as reported by CONUSS. However, fitting either the

thickness and thickness distribution or the FWHM of the QS in addition to the parameters in Table 6 within the crossover region results in nine strong correlations, emphasizing the need to fix highly correlated parameters to physically meaningful values.

## DISCUSSION

To examine a systematic effect of iron concentration on the HS and LS volumes, bulk modulus, and spin transition pressure, we fit a spin crossover equation of state to previously reported pressure-volume data of (Mg<sub>(1-x)</sub>Fe<sub>x</sub>)O ranging from  $x = 0.10$  to  $x = 0.60$  (Lin et al. 2005; Fei et al. 2007; Marquardt et al. 2009b; Zhuravlev et al. 2010; Mao et al. 2011; Chen et al. 2012) using MINUTI. Fitted spin crossover EOS parameters from X-ray diffraction data are listed in Table 7 and plotted in Figure 6.  $V_{0,HS}$  generally increases with increasing iron content while the percent difference between the HS and LS  $V_0$  appears to be roughly constant between 17 and 60 mol% FeO. The fit parameter  $K_{OT,HS}$  appears to be insensitive to iron content within this range of compositions (Jacobsen et al. 2002; Jackson et al. 2006). However, the percent difference between HS and LS  $K_{OT}$  is notably different for (Mg<sub>0.83</sub>Fe<sub>0.17</sub>)O. Fitted spin transition pressures ( $P_{tr}^*$ ) show an increase from about 50 GPa at  $x = 0.10$  to about 80 GPa for  $x = 0.60$  (Fig. 7).

Conventional Mössbauer experiments for (Mg<sub>0.50</sub>Fe<sub>0.50</sub>)O with an Ar and alcohol mixture as a pressure medium reported a transition pressure at 60 GPa (Speziale et al. 2005) while X-ray diffraction experiments for laser-annealed (Mg,Fe)O with 20, 39, and 58 mol% FeO with an NaCl pressure medium report a spin crossover at about 40, 60, and 80 GPa, respectively (Fei et

**TABLE 6.** Error correlation matrix for the fitted hyperfine parameters at 75.6 GPa (where high-spin and low-spin states coexist), acquired with CONUSS

	Fe <sub>A</sub> <sup>2+</sup> QS	Fe <sub>B</sub> <sup>2+</sup> QS	Fe <sub>A</sub> <sup>2+</sup> IS	Fe <sub>B</sub> <sup>2+</sup> IS	Fe <sub>LS</sub> <sup>2+</sup> IS
Fe <sub>A</sub> <sup>2+</sup> QS	1.000	-0.144	-0.756	0.024	0.433
Fe <sub>B</sub> <sup>2+</sup> QS	-0.144	1.000	0.276	-0.693	0.543
Fe <sub>A</sub> <sup>2+</sup> IS	-0.756	0.276	1.000	-0.146	-0.094
Fe <sub>B</sub> <sup>2+</sup> IS	0.024	-0.693	-0.146	1.000	-0.503
Fe <sub>LS</sub> <sup>2+</sup> IS	0.433	0.543	-0.094	-0.503	1.000

Notes: Thickness, thickness distribution, the QS distribution, and weight fractions of the different sites were fixed. The QS of Fe<sub>LS</sub><sup>2+</sup> was fixed to 0.

al. 2007). It is important to note that Fei et al. (2007) reported a cubic-rhombohedral phase transition at 44 GPa in (Mg,Fe)O with 58 mol% FeO. However, also using a NaCl pressure medium with laser-heating, Lin et al. (2003) find that (Mg,Fe)O with 61 mol% FeO remains cubic up to 102 GPa at 300 K and up to 2550 K. Furthermore, using a Ne pressure medium, Lin et al. (2005) observe no phase transition in (Mg,Fe)O with 60 mol% FeO at 300 K. Future Mössbauer experiments combined with X-ray diffraction measurements using a Ne pressure medium could help clarify the relationship between the rhombohedral phase transition and spin crossover. Reported spin transition pressures strongly depend on the pressure medium, pressure scale, other environmental conditions, and the criteria for assigning a particular pressure to the transition (Table 8). In the pressure range investigated, our use of Ne as a pressure medium creates a more hydrostatic environment compared to the absence of a pressure medium, NaCl, Ar, or alcohol mixtures (Klotz et al. 2009), and allows us to directly compare our results to those that used Ne (Marquardt et al. 2009b; Lin et al. 2005; Zhuravlev et al. 2010; Chen et al. 2012). Additionally, high-quality SMS measurements collected in fine (~5 GPa) pressure steps on grains of Fp48 from the same synthesis run charge allow us to resolve the presence of small low-spin weight fractions.

Computational studies have used density functional theory to predict the spin transition pressure and spin transition width for (Mg,Fe)O. When HS and LS states coexist, the mixture of states can be treated as an ideal or non-ideal solution, having additive or non-additive volumes, respectively. Although most materials are non-ideal solutions, it is often convenient to treat them as ideal solutions to simplify the calculations. Tsuchiya et al. (2006) used the LDA+U method assuming an ideal solution of HS and LS Fe atoms to calculate the spin transition pressure range for (Mg<sub>0.75</sub>Fe<sub>0.25</sub>)O. At 300 K, they predicted a spin transition pressure of 36 GPa and a narrow spin transition width of ~4 GPa (20 and 80% LS population at 34 and 38 GPa, respectively). For

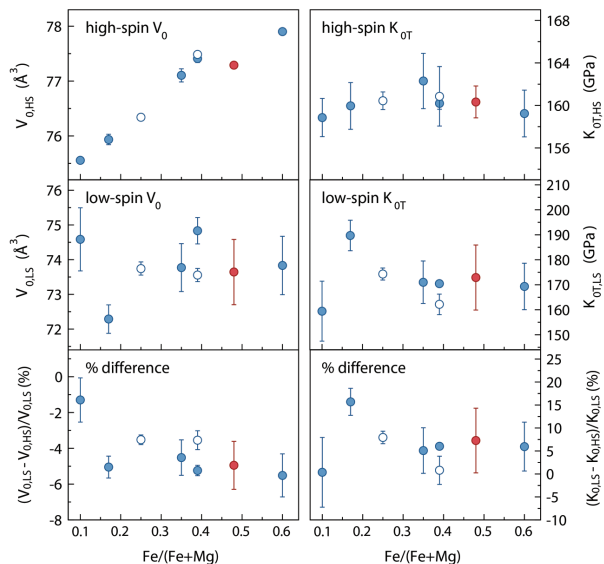


**FIGURE 6.** High-spin and low-spin zero-pressure volume and bulk modulus as a function of iron concentration, derived from a spin crossover EOS (Table 7). Fp48 is denoted by a red circle and is compared to [Mg<sub>(1-x)</sub>Fe<sub>x</sub>]O with  $x = 0.10$  (Marquardt et al. 2009b),  $x = 0.17$  (Lin et al. 2005),  $x = 0.25$  (Mao et al. 2011),  $x = 0.35$  (Chen et al. 2012),  $x = 0.39$  (Zhuravlev et al. 2010; Fei et al. 2007), and  $x = 0.60$  (Lin et al. 2005). Solid blue symbols indicate studies that used Ne as a pressure medium (Marquardt et al. 2009b; Lin et al. 2005; Chen et al. 2012; Zhuravlev et al. 2010) while open blue symbols indicate studies that used NaCl or KCl as a pressure medium (Mao et al. 2011; Fei et al. 2007). A larger concentration of iron likely results in a larger difference in volume between HS and LS (Mg,Fe)O, whereas  $K_0$  for the HS state appears to be insensitive to iron concentration in (Mg,Fe)O for these compositions.

(Mg<sub>0.8125</sub>Fe<sub>0.1875</sub>)O, Holmström and Stixrude (2015) performed molecular dynamics simulations within density functional theory, using the GGA+U method. Assuming a non-ideal solution of HS and LS Fe atoms, the mixed spin phase is stabilized even at low temperatures. At 300 K, they predict a spin transition pressure of 65 GPa with a broad spin transition width of ~50 GPa (20 and 80% LS population at approximately 45 and 95 GPa). Using the same percentage range of LS population, the spin transition widths determined from XRD measurements using MINUTI are 8.2 GPa for (Mg<sub>0.83</sub>Fe<sub>0.17</sub>)O and 15.9 GPa for (Mg<sub>0.75</sub>Fe<sub>0.25</sub>)O (Fig. 7 inset). Thus, it appears that using an ideal or non-ideal solution of HS and

**TABLE 7.** Spin crossover equation of state parameters determined from MINUTI using a third-order Birch Murnaghan equation of state and fixing  $K'_{0T,LS}$  to 4

Composition	$V_{0,HS}$ (Å <sup>3</sup> )	$V_{0,LS}$ (Å <sup>3</sup> )	$K_{0T,HS}$ (GPa)	$K_{0T,LS}$ (GPa)	$K'_{0T,HS}$	$P_{tr}$ (GPa)	$P_{tr}$ width (GPa)	References
(Mg <sub>0.90</sub> Fe <sub>0.10</sub> )O	75.55(4)	74.59(91)	159(2)	159(12)	3.96(14)	52.1(1.9)	2.3	Marquardt et al. (2009b)
(Mg <sub>0.83</sub> Fe <sub>0.17</sub> )O	75.94(10)	72.29(41)	160(2)	190(6)	4.04(16)	49.2(1.3)	8.2	Lin et al. (2005)
(Mg <sub>0.75</sub> Fe <sub>0.25</sub> )O	76.34(0)	73.74(19)	160(1)	174(2)	4.28(6)	62.6(7)	15.9	Mao et al. (2011)
(Mg <sub>0.65</sub> Fe <sub>0.35</sub> )O	77.10(12)	73.77(69)	162(3)	171(9)	3.99(15)	63.7(1.7)	13.3	Chen et al. (2012)
(Mg <sub>0.61</sub> Fe <sub>0.39</sub> )O	77.49(3)	74.83(38)	161(3)	162(4)	4.25(24)	56.6(1.5)	17.2	Fei et al. (2007)
(Mg <sub>0.61</sub> Fe <sub>0.39</sub> )O	77.41(7)	73.56(19)	160(1)	170(2)	4.07(5)	73.5(1.0)	10.3	Zhuravlev et al. (2010)
(Mg <sub>0.49</sub> Fe <sub>0.48</sub> )O <sup>a</sup>	77.29(0)	73.64(94)	160(2)	173(13)	4.12(14)	68.8(2.7)	18.4	This study
(Mg <sub>0.40</sub> Fe <sub>0.60</sub> )O	77.90(4)	73.83(84)	159(2)	169(9)	3.82(14)	78.6(5.1)	25.1	Lin et al. (2005)

Notes: For  $x = 0.17$  to  $x = 0.60$ , the data was fitted with the procedure described in Table 2. For  $x = 0.10$ , where  $K_{05,HS}$  was directly measured with Brillouin scattering (Marquardt et al. 2009b), a prior of 161.4 GPa (the measured  $K_{05,HS}$ ) with a prior window of  $\pm 3$  was used, accounting for a difference between the isothermal and adiabatic bulk modulus. The spin transition width ( $P_{tr}$  width) was determined from the 20/80% completion of the volume change due to the HS to LS transition, fitted with MINUTI.

<sup>a</sup> See Experimental methods for chemical analysis. The full composition as determined from microprobe analysis is (Mg<sub>0.490(3)</sub>Fe<sub>0.483(2)</sub>Ti<sub>0.027(5)</sub>)O.



LS states either underestimates or overestimates the spin transition width observed experimentally at 300 K.

### IMPLICATIONS

An understanding of the effect of iron on the density, crystal structure, and magnetic behavior of ferroperricite is important for understanding the presence of (Mg,Fe)O in lower-mantle phase assemblages. To examine the effect of iron concentration in (Mg,Fe)O on geophysically relevant properties, we have calculated

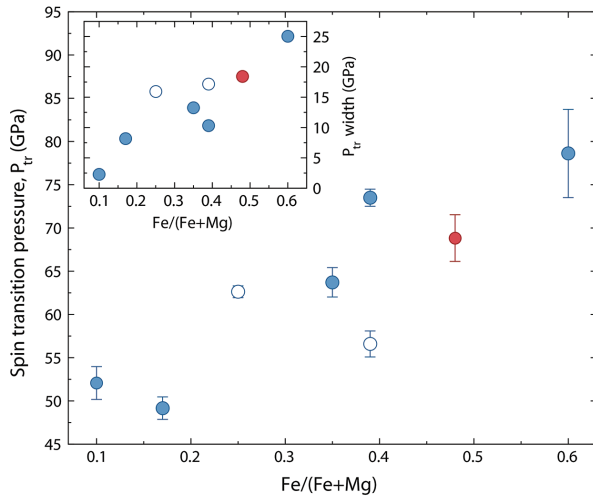


**FIGURE 7.** Spin transition pressure of  $(\text{Mg}_{1-x}\text{Fe}_x)\text{O}$  as a function of iron concentration, fitted with MINUTI. The inset shows the spin transition widths, determined from the 20–80% volume drop. References for symbols are the same as in Figure 6.

the bulk modulus, density, and bulk sound velocities up to 140 GPa at 300 K for (Mg,Fe)O with 17, 48, and 60 mol% FeO, with uncertainties that reflect the equations of state parameter correlations (Figs. 8–10). The significant softening of the bulk modulus and bulk sound velocities in the spin crossover region is a direct result of the compression behavior at 300 K, but is unlikely to persist with the same magnitude at high temperatures (Sturhahn et al. 2005; Tsuchiya et al. 2006; Komabayashi et al. 2010; Mao et al. 2011; Holmström and Stixrude 2015). As shown previously,

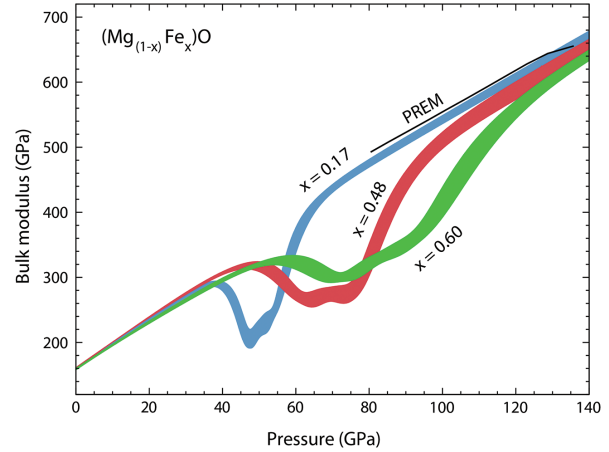


**FIGURE 8.** Isothermal bulk modulus as a function of pressure for  $(\text{Mg}_{1-x}\text{Fe}_x)\text{O}$  at 300 K where blue is  $x = 0.17$  (Lin et al. 2005), red is  $x = 0.48$  (this study), and green is  $x = 0.60$  (Lin et al. 2005), fitted with MINUTI. Other compositions were omitted for clarity, as there is significant overlap between data sets. The preliminary reference model (PREM) (Dziewonski and Anderson 1981) is shown in black.

**TABLE 8.** Experimental studies on the reported spin transition pressure ( $P_{tr}$ ) range of iron in (Mg,Fe)O at 300 K

Composition	$P_{tr}$ range (GPa)	Method	Pressure medium	Pressure scale	References
$(\text{Mg}_{0.95}\text{Fe}_{0.05})\text{O}$	46–55	X-ray emission	none	ruby	Lin et al. (2007)
$(\text{Mg}_{0.90}\text{Fe}_{0.10})\text{O}$	45–63	X-ray diffraction	Ne	ruby	Marquardt et al. (2009b)
$(\text{Mg}_{0.88}\text{Fe}_{0.12})\text{O}$	51–60	Optical absorption	Ar	ruby	Keppeler et al. (2007)
$(\text{Mg}_{0.83}\text{Fe}_{0.17})\text{O}$	60–70	X-ray emission	none	ruby	Badro et al. (2003)
$(\text{Mg}_{0.83}\text{Fe}_{0.17})\text{O}$	57–75	X-ray diffraction	Ne	Pt	Lin et al. (2005)
$(\text{Mg}_{0.80}\text{Fe}_{0.20})\text{O}$	40–70 <sup>a</sup>	Conventional Mössbauer	none	ruby	Speziale et al. (2005)
$(\text{Mg}_{0.80}\text{Fe}_{0.20})\text{O}$	55–105	Conventional Mössbauer	none	ruby	Kantor et al. (2006)
$(\text{Mg}_{0.80}\text{Fe}_{0.20})\text{O}$	35–45	X-ray diffraction	NaCl	NaCl	Fei et al. (2007)
$(\text{Mg}_{0.75}\text{Fe}_{0.25})\text{O}$	54–67	X-ray emission	NaCl	ruby	Lin et al. (2005)
$(\text{Mg}_{0.75}\text{Fe}_{0.25})\text{O}$	55–65	Optical absorption	Ar, Ne	ruby	Goncharov et al. (2006)
$(\text{Mg}_{0.75}\text{Fe}_{0.25})\text{O}$	52–70	Synchrotron Mössbauer	KCl	ruby	Lin et al. (2006a)
$(\text{Mg}_{0.75}\text{Fe}_{0.25})\text{O}$	52–78 <sup>b</sup>	X-ray diffraction	KCl, NaCl	Au	Mao et al. (2011)
$(\text{Mg}_{0.65}\text{Fe}_{0.35})\text{O}$	49–79	X-ray diffraction	Ne	ruby	Chen et al. (2012)
$(\text{Mg}_{0.61}\text{Fe}_{0.39})\text{O}$	60–66	X-ray diffraction	NaCl	NaCl	Fei et al. (2007)
$(\text{Mg}_{0.61}\text{Fe}_{0.39})\text{O}$	65–77	X-ray diffraction	Ne	ruby	Zhuravlev et al. (2010)
$(\text{Mg}_{0.49}\text{Fe}_{0.48})\text{O}$	59–78 <sup>c</sup>	X-ray diffraction	Ne	ruby	This study
$(\text{Mg}_{0.49}\text{Fe}_{0.48})\text{O}$	52–85 <sup>d</sup>	Synchrotron Mössbauer	Ne	ruby	This study
$(\text{Mg}_{0.50}\text{Fe}_{0.50})\text{O}$	60–75 <sup>e</sup>	Conventional Mössbauer	none	ruby	Speziale et al. (2005)
$(\text{Mg}_{0.42}\text{Fe}_{0.58})\text{O}$	75–85	X-ray diffraction	NaCl	NaCl	Fei et al. (2007)
$(\text{Mg}_{0.40}\text{Fe}_{0.60})\text{O}$	84–102	X-ray emission	NaCl	ruby	Lin et al. (2005)
$(\text{Mg}_{0.20}\text{Fe}_{0.80})\text{O}$	80–100	Conventional Mössbauer	none	ruby	Speziale et al. (2005)
$(\text{Mg}_{0.16}\text{Fe}_{0.84})\text{O}$	100–121	Synchrotron Mössbauer	boron epoxy	ruby	Wicks et al. (2010)
$\text{Fe}_{0.94}\text{O}$	90–140	Conventional Mössbauer	none	ruby	Pasternak et al. (1997)

Notes: The pressure mediums, pressure scales, and definition of  $P_{tr}$  and  $P_{tr}$  range differ between these studies. Some of these studies did not use a pressure medium (Pasternak et al. 1997; Badro et al. 2003; Kantor et al. 2006; Speziale et al. 2005; Lin et al. 2007).  $P_{tr}$  is a function of iron concentration and is likely sensitive to hydrostatic conditions.

<sup>a</sup> Transition pressure at 6 K.

<sup>b</sup> A KCl pressure medium was used below 60 GPa, whereas NaCl was used above 60 GPa.

<sup>c</sup> Range from 20–80% volume change, as discussed in the text.

<sup>d</sup> Range from 19–76% LS population.

<sup>e</sup> Transition pressure at 10 K.

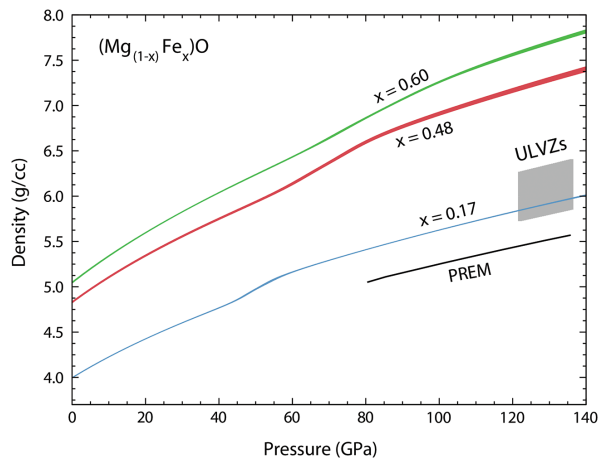


**FIGURE 9.** Density as a function of pressure for  $(\text{Mg}_{(1-x)}\text{Fe}_x)\text{O}$  at 300 K. An estimate for ULVZs is shown in gray (Rost et al. 2005). The density of Fp48 was corrected for natural  $^{57}\text{Fe}$  abundance. Color scheme same as in Figure 8.

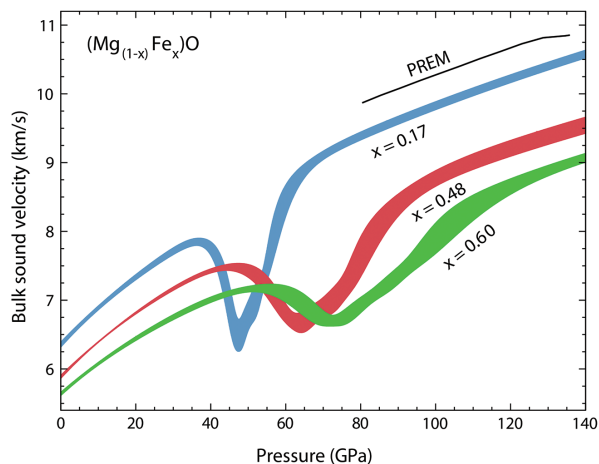


**FIGURE 10.** Bulk sound velocity as a function of pressure for  $(\text{Mg}_{(1-x)}\text{Fe}_x)\text{O}$  at 300 K. The bulk sound velocity for Fp48 was corrected for natural  $^{57}\text{Fe}$  abundance. Color scheme same as in Figure 8.

the effect of the gradual density crossover along a typical geotherm contributes an additional “spin buoyancy” to mantle materials containing ferropericlase (Bower et al. 2009).

At the base of the mantle, 5–40 km thick patches of ultralow-velocity zones (ULVZs) have been detected, often located at the edges of large low shear velocity provinces (LLSVPs) (Garnero and Helmberger 1996; McNamara et al. 2010; Rost 2013; Brown et al. 2015). Although many ULVZs are associated with LLSVPs and are thought to contain partial melt (Williams et al. 1998), some appear uncorrelated with LLSVPs and hotspots on Earth’s surface (Sun et al. 2013). These particular patches might be best explained by an enrichment of iron-rich  $(\text{Mg,Fe})\text{O}$  (Labrosse et al. 2007; Wicks et al. 2010; Bower et al. 2011; Rost 2013). To explain ULVZs by the presence of  $(\text{Mg,Fe})\text{O}$ , the resulting mixture must have topographic relief and wave speed reductions that match seismic observations. Distinct ULVZs at the base of

the mantle have been explored in numerical convection models using a range of chemical density anomalies, where the buoyancy number of such a layer is determined in part by its thermal equation of state and controls its evolved topography (Bower et al. 2011). The systematic analysis presented here demonstrates that the enrichment of iron in  $(\text{Mg,Fe})\text{O}$  increases the pressure and width of the spin crossover (see Fig. 7 and Table 8). Therefore, iron-rich  $(\text{Mg,Fe})\text{O}$  at the core-mantle boundary would likely contain a significant fraction of high-spin (less dense) iron, contributing a positive buoyancy to promote observable topographic relief. The combination of the results presented here and additional constraints on the phase equilibria, wave velocities, and thermoelasticity of candidate phase assemblages will further narrow the range of plausible explanations of multi-scale structures in the deep mantle.

## ACKNOWLEDGMENTS

We thank E.E. Alp and W. Bi for the isomer shift measurement of the reference stainless steel foil. We are thankful to NSF-EAR-CAREER-0956166, NSF-CSEDI-EAR-1161046, and COMPRES, which partially supports operations at Sector 3 (APS), the Mössbauer Laboratory (APS), and Beamline 12.2.2 (ALS). Ambient X-ray diffraction experiments at 11-BM of APS were made possible by Saul Lapidus and Lynn Ribaud. Microprobe analyses at Caltech were partially funded by MRSEX Program of the NSF under DMR-0080065. Ruby fluorescence measurements for the SMS experiments were conducted at GSE-CARS. Use of the Advanced Photon Source is supported by the U.S. DOE, Office of Science (DE-AC02-06CH11357). The Advanced Light Source is supported by the U.S. DOE, Office of Science (DE-AC02-05CH11231). We thank two anonymous reviewers for their thoughtful comments.

## REFERENCES CITED

- Antonangeli, D., Siebert, J., Araçne, C.M., Farber, D.F., Bosak, A., Hoesch, M., Krisch, M., Ryerson, F.J., Fiquet, G., and Badro, J. (2011) Spin crossover in ferropericlase at high pressure: A seismologically transparent transition? *Science*, 331, 64–67.
- Auzende, A.L., Badro, J., Ryerson, F.J., Weber, P.K., Fallon, S.J., Addad, A., Siebert, J., and Fiquet, G. (2008) Element partitioning between magnesium silicate perovskite and ferropericlase: New insights into bulk lower-mantle geochemistry. *Earth and Planetary Science Letters*, 269, 164–174.
- Badro, J., Fiquet, G., Guyot, F., Rueff, J.P., Struzhkin, V.V., Vanko, G., and Monaco, G. (2003) Iron partitioning in Earth’s mantle: toward a deep lower mantle discontinuity. *Science*, 300, 789–791.
- Bower, D.J., Gurnis, M., Jackson, J.M., and Sturhahn, W. (2009) Enhanced convection and fast plumes in the lower mantle induced by the spin transition in ferropericlase. *Geophysical Research Letters*, 36, L10306.
- Bower, D.J., Wicks, J.K., Gurnis, M., and Jackson, J.M. (2011) A geodynamic and mineral physics model of a solid-state ultralow-velocity zone. *Earth and Planetary Science Letters*, 303, 193–202.
- Brown, S.P., Thorne, M.S., Miyagi, L., and Rost, S. (2015) A compositional origin to ultralow-velocity zones. *Geophysical Research Letters*, 42, 1039–1045.
- Chen, B., Jackson, J.M., Sturhahn, W., Zhang, D., Zhao, J., Wicks, J.K., and Murphy, C.A. (2012) Spin crossover equation of state and sound velocities of  $(\text{Mg}_{0.65}\text{Fe}_{0.35})\text{O}$  ferropericlase to 140 GPa. *Journal of Geophysical Research*, 117, B08208.
- Dobson, D.P., and Brodholt, J.P. (2005) Subducted banded iron formations as a source of ultralow-velocity zones at the core-mantle boundary. *Nature*, 434, 371–374.
- Duffy, T.S., and Ahrens, T.K. (1993) Thermal expansion of mantle and core materials at very high pressures. *Geophysical Research Letters*, 20, 1103–1106.
- Dziewonski, A.M., and Anderson, D.L. (1981) Preliminary reference Earth model. *Physics of the Earth and Planetary Interiors*, 25, 297–356.
- Fei, Y., and Mao, H.K. (1994) In situ determination of the NiAs phase of FeO at high pressure and temperature. *Science*, 266, 1678–1680.
- Fei, Y., Zhang, L., Corgne, A., Watson, H., Ricolleau, A., Meng, Y., and Prakapenka, V. (2007) Spin transition and equations of state of  $(\text{Mg, Fe})\text{O}$  solid solutions. *Geophysical Research Letters*, 34, L17307.
- Fischer, R.A., Campbell, A.J., Shofner, G.A., Lord, O.T., Dera, P., and Prakapenka, V.B. (2011) Equation of state and phase diagram of FeO. *Earth and Planetary Science Letters*, 304, 496–502.
- Fujii, A., Kondo, T., Taniguchi, T., and Sakaiya, T. (2011) Néel transition in  $(\text{Mg, Fe})\text{O}$ : A possible change of magnetic structure. *American Mineralogist*, 96, 329–332.
- Garnero, E.J., and Helmberger, D.V. (1996) Seismic detection of a thin laterally varying boundary layer at the base of the mantle beneath the central Pacific. *Geophysical Research Letters*, 23, 977–980.
- Goncharov, A.F., Struzhkin, V.V., and Jacobsen, S.D. (2006) Reduced radiative conductivity of low-spin  $(\text{Mg, Fe})\text{O}$  in the lower mantle. *Science*, 312, 1205–1208.

- Hammersley, A.O., Svensson, S.O., Hanfland, M., Fitch, A.N., and Hausermann, D. (1996) Two-dimensional detector software: from real detector to idealized image or two-theta scan. *High Pressure Research*, 14, 235–248.
- Holmström, E., and Stixrude, L. (2015) Spin crossover in ferropericlase from first-principles molecular dynamics. *Physical Review Letters*, 114, 117202.
- Jackson, J.M., Sinogeikin, S.V., Jacobsen, S.D., Reichmann, H.J., Mackwell, S.J., and Bass, J.D. (2006) Single-crystal elasticity and sound velocities of  $(\text{Mg}_{0.94}\text{Fe}_{0.06})\text{O}$  ferropericlase to 20 GPa. *Journal of Geophysical Research*, 111, B09203.
- Jacobsen, S.D., Reichmann, H.J., Spetzler, H., Mackwell, S.J., Smyth, J.R., Angel, R.J., and McCammon, C.A. (2002) Structure and elasticity of single-crystal  $(\text{Mg,Fe})\text{O}$  and a new method of generating shear waves for gigahertz ultrasonic interferometry. *Journal of Geophysical Research*, 107, 5867–5871.
- Jacobsen, S.D., Holl, C.M., Adams, K.A., Fischer, R.A., Martin, E.S., Bina, C.R., Lin, J., Prakapenka, V.B., Kubo, A., and Dera, P. (2008) Compression of single-crystal magnesium oxide to 118 GPa and a ruby pressure gauge for helium pressure media. *American Mineralogist*, 93, 1823–1828.
- Kantor, I., Dubrovinsky, L., McCammon, C., Kantor, A., Pascarelli, S., Aquilanti, G., Crichton, W., Mattesini, M., Ahuja, R., Almeida, J., and Urusov, V. (2006) Pressure-induced phase transition in  $(\text{Mg}_{0.8}\text{Fe}_{0.2})\text{O}$  ferropericlase. *Physics and Chemistry of Minerals*, 33, 35–44.
- Keppeler, H., Kantor, I.Y., and Dubrovinsky, L.S. (2007) Optical absorption spectra of ferropericlase to 84 GPa. *American Mineralogist*, 92, 433–436.
- Klotz, S., Chervin, J.C., Munsch, P., and Marchand, G.L. (2009) Hydrostatic limits of 11 pressure transmitting media. *Journal of Physics D: Applied Physics*, 42, 075413.
- Kobayashi, Y., Kondo, T., Ohtani, E., Hirao, N., Miyajima, N., Yagi, T., Nagase, T., and Kikegawa, T. (2005) Fe-Mg partitioning between  $(\text{Mg,Fe})\text{SiO}_3$  post-perovskite, perovskite, and magnesiowüstite in the Earth's lower mantle. *Geophysical Research Letters*, 32, L19301.
- Komabayashi, T., Hirose, K., Nagaya, Y., Sugimura, E., and Ohishi, Y. (2010) High-temperature compression of ferropericlase and the effect of temperature on iron spin transition. *Earth and Planetary Science Letters*, 297, 691–699.
- Labrosse, S., Hernlund, J.W., and Coltice, N. (2007) A crystallizing dense magma ocean at the base of the Earth's mantle. *Nature*, 450, 866–869.
- Lin, J.F., Heinz, D.L., Mao, H.K., Hemley, R.J., Devine, J.M., Li, J., and Shen, G. (2003) Stability of magnesiowüstite in Earth's lower mantle. *Proceedings of the National Academy of Sciences*, 100, 4405–4408.
- Lin, J.F., Struzhkin, V.V., Jacobsen, S., Hu, M.Y., Chow, P., Kung, J., Liu, H., Mao, H., and Hemley, R.J. (2005) Spin transition of iron in magnesiowüstite in the Earth's lower mantle. *Nature*, 436, 377–380.
- Lin, J.F., Gavriluk, A.G., Struzhkin, V.V., Jacobsen, S.D., Sturhahn, W., Hu, M.Y., Chow, P., and Yoo, C.S. (2006a) Pressure-induced electronic spin transition of iron in magnesiowüstite- $(\text{Mg,Fe})\text{O}$ . *Physical Review B*, 73, 113107.
- Lin, J.F., Jacobsen, S.D., Sturhahn, W., Jackson, J.M., Zhao, J., and Yoo, C.S. (2006b) Sound velocities of ferropericlase in the Earth's lower mantle. *Geophysical Research Letters*, 33, L22304.
- Lin, J.F., Struzhkin, V.V., Gavriluk, A.G., and Lyubutin, I. (2007) Comment on "Spin crossover in  $(\text{Mg,Fe})\text{O}$ : a Mössbauer effect study with an alternative interpretation of X-ray emission spectroscopy data". *Physics Review*, 75, 177102.
- Manga, M., and Jeanloz, R. (1996) Implications of a metal-bearing chemical boundary layer in D" for mantle dynamics. *Geophysical Research Letters*, 23, 3091–3094.
- Mao, H.K., Shu, J., Fei, Y., Hu, J., and Hemley, R.J. (1996) The wüstite enigma. *Physics of the Earth and Planetary Interiors*, 96, 135–145.
- Mao, W., Shu, J., Hu, J., Hemley, R., and Mao, H.K. (2002) Displacive transition in magnesiowüstite. *Journal of Physics: Condensed Matter*, 14, 11349.
- Mao, W.L., Shen, G., Prakapenka, V.B., Meng, Y., Campbell, A.J., Heinz, D.L., Shu, J., Hemley, R.J., and Mao, H. (2004) Ferromagnesian postperovskite silicates in the D" layer of the Earth. *Proceedings of the National Academy of Sciences*, 101, 15867–15869.
- Mao, Z., Lin, J.F., Liu, J., and Prakapenka, V.B. (2011) Thermal equation of state of lower-mantle ferropericlase across the spin crossover. *Geophysical Research Letters*, 38, L23308.
- Marquardt, H., Speziale, S., Reichmann, H.J., Frost, D.J., Schilling, F.R., and Garnero, E.J. (2009a) Elastic shear anisotropy of ferropericlase in Earth's lower mantle. *Science*, 324, 224–226.
- Marquardt, H., Speziale, S., Reichmann, H.J., Frost, D.J., and Schilling, F.R. (2009b) Single-crystal elasticity of  $(\text{Mg}_{0.9}\text{Fe}_{0.1})\text{O}$  to 81 GPa. *Earth and Planetary Science Letters*, 287, 345–352.
- McNamara, A.K., Garnero, E.J., and Rost, S. (2010) Tracking deep mantle reservoirs with ultralow-velocity zones. *Earth and Planetary Science Letters*, 299, 1–9.
- Mosenfelder, J.L., Asimow, P.D., Frost, D.J., Rubie, D.C., and Ahrens, T.J. (2009) The  $\text{MgSiO}_3$  system at high pressure: Thermodynamic properties of perovskite, postperovskite, and melt from global inversion of shock and static compression data. *Journal of Geophysical Research*, 114, B01203.
- Pasternak, M.P., Taylor, R.D., Jeanloz, R., Li, X., Nguyen, J.H., and McCammon, C.A. (1997) High pressure collapse of magnetism in  $\text{Fe}_{0.94}\text{O}$ : Mössbauer spectroscopy beyond 100 GPa. *Physical Review Letters*, 79, 5046–5049.
- Persson, K., Bengtson, A., Ceder, G., and Morgan, D. (2006) Ab initio study of the composition dependence of the pressure induced spin transition in the  $(\text{Mg}_{1-x}\text{Fe}_x)$ . *Geophysical Research Letters*, 33, L16306.
- Rost, S. (2013) Core-mantle boundary landscapes. *Nature*, 6, 89–90.
- Rost, S., Garnero, E.J., Williams, Q., and Manga, M. (2005) Seismological constraints on a possible plume root at the core-mantle boundary. *Nature*, 435, 666–669.
- Sakai, T., Ohtani, E., Terasaki, H., Sawada, N., Kobayashi, Y., Miyahara, M., Nishijima, M., Hirao, N., Ohishi, Y., and Kikegawa, T. (2009) Fe-Mg partitioning between perovskite and ferropericlase in the lower mantle. *American Mineralogist*, 94, 921–925.
- Sinmyo, R., Hirose, K., Nishio-Hamane, D., Seto, Y., Fujino, K., Sata, N., and Ohishi, Y. (2008) Partitioning of iron between perovskite/postperovskite and ferropericlase in the lower mantle. *Journal of Geophysical Research*, 113, B11204.
- Speziale, S., Milner, A., Lee, V.E., Clark, S.M., Pasternak, M.P., and Jeanloz, R. (2005) Iron spin transition in Earth's mantle. *Proceedings of the National Academy of Sciences*, 102, 17918–17922.
- Sturhahn, W. (2000) CONUSS and PHOENIX: Evaluation of nuclear resonant scattering data. *Hyperfine Interactions*, 125, 149–172.
- (2015) MINUTI open source software, version 1.1.2, www.nrxs.com.
- Sturhahn, W., Jackson, J.M., and Lin, J.F. (2005) The spin state of iron in minerals of Earth's lower mantle. *Geophysical Research Letters*, 32, L12307.
- Sun, D., Helmenberger, D.V., Jackson, J.M., Clayton, R.W., and Bower, D.J. (2013) Rolling hills on the core-mantle boundary. *Earth and Planetary Science Letters*, 361, 333–342.
- Toellner, T.S. (2000) Monochromatization of synchrotron radiation for nuclear resonant scattering experiments. *Hyperfine Interactions*, 125, 3–28.
- Tsuchiya, T., Wentzcovitch, R.M., da Silva, C.R.S., and de Gironcoli, S. (2006) Spin transition in magnesiowüstite in Earth's lower mantle. *Physical Review Letters*, 96, 198501.
- Wicks, J.K., Jackson, J.M., and Sturhahn, W. (2010) Very low sound velocities in iron-rich  $(\text{Mg,Fe})\text{O}$ : Implications for the core-mantle boundary region. *Geophysical Research Letters*, 37, L15304.
- Wicks, J.K., Jackson, J.M., Sturhahn, W., Zhuravlev, K.K., Tkachev, S.N., and Prakapenka, V.B. (2015) Thermal equation of state and stability of  $(\text{Mg}_{0.6}\text{Fe}_{0.4})\text{O}$ . *Physics of the Earth and Planetary Interiors*, 249, 28–42.
- Williams, Q., and Garnero, E.J. (1996) Seismic evidence for partial melt at the base of Earth's mantle. *Science*, 273, 1528–1530.
- Williams, Q., Revenaugh, J., and Garnero, E. (1998) A correlation between ultra-low basal velocities in the mantle and hot spots. *Science*, 281, 546–549.
- Wojdyr, M. (2010) Fityk: a general-purpose peak fitting program. *Journal of Applied Crystallography*, 43, 1126–1128.
- Yagi, T., Suzuki, T., and Akimoto, S.I. (1985) Static compression of wüstite ( $\text{Fe}_{0.98}\text{O}$ ) to 120 GPa. *Journal of Geophysical Research*, 90, 8784–8788.
- Zhang, Z., Church, N., Lappe, S.C., Reinecker, M., Fuih, A., Saines, P.J., Harrison, R.J., Schranz, W., and Carpenter, M.A. (2012) Elastic and anelastic anomalies associated with the antiferromagnetic ordering transition in wüstite,  $\text{Fe}_x\text{O}$ . *Journal of Physics: Condensed Matter*, 24, 215404.
- Zhang, D., Jackson, J.M., Zhao, J., Sturhahn, W., Alp, E.E., Toellner, T.S., and Hu, M. (2015) Fast temperature spectrometer for samples under extreme conditions. *Review of Scientific Instruments*, 86, 013105.
- Zhuravlev, K.K., Jackson, J.M., Wolf, A.S., Wicks, J.K., Yan, J., and Clark, S.M. (2010) Isothermal compression behavior of  $(\text{Mg,Fe})\text{O}$  using neon as a pressure medium. *Physics and Chemistry of Minerals*, 37, 465–474.

MANUSCRIPT RECEIVED JULY 24, 2015

MANUSCRIPT ACCEPTED DECEMBER 24, 2015

MANUSCRIPT HANDLED BY MARTIN KUNZ